Optik - International Journal for Light and Electron Optics 302 (2024) 171659

Contents lists available at ScienceDirect

Optik

journal homepage: www.elsevier.com/locate/ijleo

# Investigating a Pb-free n-i-p perovskite solar cell with BFCO absorber using SCAPS-1D

Nassim Ahmed Mahammedi [a,b,*], Afif Benameur [c], Hamza Gueffaf [b], Boualem Merabet [c], Osman Murat Ozkendir [d], Shin-Ichiro Sato [e]

[a] Department of Physics, Stockholm University, Stockholm 106 91, Sweden
[b] Laboratoire Étude et Développement des Matériaux Semi-conducteur et Diélectriques (LEDMaScD.), Ammar Télidji University of Laghouat, BP 37G, Laghouat 03000, Algeria
[c] Faculty of Sciences & Technology, Mustapha Stambouli University, Mascara 29000, Algeria
[d] Department of Natural & Mathematical Sciences, Faculty of Engineering, Tarsus University, Turkey
[e] National Institutes for Quantum Science and Technology, Takasaki, Gunma 370-1292, Japan

ARTICLE INFO

*Keywords:*
Solar cell simulation
SCAPS-1D
Perovskite
Thin film
BFCO
PV parameters

ABSTRACT

In recent years, perovskite solar cells (PSCs) have gained significant attention as highly efficient photovoltaic (PV) devices. Despite achieving record levels of power conversion efficiency (PCE), the commercialization of Pb-based PSCs has been hindered by factors such as lead toxicity and stability. As a potential alternative, Pb-free Bi-based all-inorganic PSCs show promising efficiency. In this study, we utilized the Solar Cell Capacitance Simulator (SCAPS-1D) to optimize a $Bi_2FeCrO_6$-based (BFCO) PSC and analyzed the impact of absorber thickness, doping concentration, and external parameters on its PV performance. We have found that an optimized n-i-p architecture with an absorber thickness of 150 nm yielded a maximum PCE of 7% at ambient temperature (with open-circuit voltage, short-circuit current density, and fill factor of 1.12 V, 12 mA/cm$^2$, and 53.7%, respectively). Furthermore, we found that decreasing the defects density $N_t$ of the BFCO layer below $10^{13}$ cm$^{-3}$ could increase the PCE to above 10%. Our findings also revealed that the temperature had a negative effect on the solar cell, and the optimum conditions were at ambient 300 K. These results are encouraging for advancing Pb-free PSCs and enhancing their design and integration into tandem SCs.

## 1. Introduction

PV energy is increasingly becoming one of the most reliable and affordable sources of electricity as conversion efficiency continues to increase and prices fall. This is due to the large-scale manufacturing and distribution, together with a growing environmental consciousness among governments and communities, enabling the installation of multi gigawatt-scale PV plants worldwide [1]. Silicon, the key material behind this flourishing business, dominates not only the PV sector, but also the fields of microelectronics, photonics and quantum computing. This dominance is attributed to its many features such as abundance, mature technology, low-cost processing, stable oxide $SiO_2$, cheap wafers and raw materials [2]. However, in the PV landscape, Si could only be challenged by its inherent drawbacks, such as the weak light absorption related to its indirect bandgap and the difficult recyclability. This paved the way

* Corresponding author at: Department of Physics, Stockholm University, Stockholm 106 91, Sweden.
*E-mail address:* nassim.mahammedi@fysik.su.se (N.A. Mahammedi).

https://doi.org/10.1016/j.ijleo.2024.171659
Received 23 May 2023; Received in revised form 18 January 2024; Accepted 25 January 2024
Available online 29 January 2024
0030-4026/© 2024 The Author(s). Published by Elsevier GmbH. This is an open access article under the CC BY license (http://creativecommons.org/licenses/by/4.0/).

for the emergence of other alternatives that could, at some extent, overcome those issues [3]. Direct bandgap semiconductors like CIGS [4], CdTe [5] and III-V [6] allowed the fabrication of thin film solar cells alongside other emergent technologies like organics [7], dye-sensitized [8] and perovskite solar cells [9], all belonging to what's known as the second- and third-generation PVs. Among these promising technologies, the perovskite branch, have become one of the most investigated PV branches within the last two decades [10–12].

Perovskites, typically used as thin films in PSCs, are attracting growing attention, due to their astonishing physical properties [13], ever-increasing conversion efficiencies [14–19], low-cost processing [20], direct bandgaps [21], low exciton binding energy [22], and enhanced light absorption [23]. For commercialization of PSCs, it is crucial to achieve higher power conversion efficiencies (PCE) [24], long-term stability [25], and low toxicity [26,27]. Inorganic perovskites have been shown to be more stable compared to their organic counterparts under harsh conditions, including light, heat, and electron beam exposures [28]. Interestingly, amid full inorganic perovskites, bismuth-based double perovskites (DPs) are envisaged to develop non-toxic, narrow direct bandgap with suitable stability and promising properties for enhanced PCEs [29]. Among them, the metastable multiferroic $Bi_2FeCrO_6$ (BFCO) stands out as a tunable direct bandgap ($E_g$) DP with enhanced light absorption and carrier mobilities. Compared to conventional FE materials, multiferroic systems, in which magnetic order and ferroelectricity coexist, exhibit strong electron−electron interactions that are able to modulate their magnetization and tune their bandgaps [30]. BFCO has been explored for its potential use in thin film PSCs [12, 30–32]. In this regard, a significant PV effect has been observed in BFCO thin films under monochromatic illumination at 635 nm (1.5 mW.cm$^{-2}$), exhibiting a high photocurrent density ($J_{PH}$) at 0 V bias and an open-circuit voltage ($V_{OC}$) of ~0.6 V [33]. BFCO adopts a double perovskite structure with a random occupancy of $Fe^{3+}$ and $Cr^{3+}$ on the B-site due to similar ionic radii of $Fe^{3+}$ (r=0.654Å) and $Cr^{3+}$ (r=0.615Å), which reduces the symmetry of the space group to R3 as compared with BFO [12]. The BFCO's ferroelectric properties also open up the possibility of its usage in ferroelectric-photovoltaic (FE-PV) devices. Herein, unlike conventional semiconductors, PV cells based on FE materials used either as absorbers and/or photoelectrodes, could achieve greater $V_{OC}$ with values higher than their bandgaps due to the remnant FE polarization-induced electric fields which effectively separate the electron−hole pairs. This polarization-induced field, in contrast to the built-in electric field that forms in regular p-n junctions, also modulates the chemical potential and surface band bending of FE material-based photoelectrodes, thereby allowing to tailor the PCE [30]. The ferroelectricity in BFCO arises from the 6 $s^2$ lone pair on $Bi^{3+}$ ions, where atoms move off-center to form the electric dipole moment. *S. Li et al.* stated that the bandgap of BFCO is theoretically defined by the difference between the Cr3d –O2p hybrids in the valence band and the empty Fe-3d conduction band. Altering $E_g$ requires the modification of the transition metal-oxygen (TM-O) bond lengths and their interaction energies; that is, the hybridization energy and the Coulomb repulsion [34]. In a theoretical investigation, by *L. Wei et al.* have reported that tetragonal-BFCO has a narrow $E_g$=0.78 eV, due to contributions Fe-3d/Bi-6p and Cr-3d/O-2p states, and a large polarization of 60.7μC.cm$^{-2}$ [35]. However, such a narrow $E_g$ values are far from the ideal Shockley–Queisser limit known to be equal to 1.34 eV [36], clearly limiting $V_{CO}$ for PSCs, and $E_g$-tuning likely plays a key role in further improvement of PCEs. *R. Nechache et al.* tuned the $E_g$ of BFCO in the range 1.4 eV-2.4 eV by manipulating the Fe/Cr cation ordering and ordered domain sizes, and proved an efficiency of 8.1% under 100 mW.cm$^{-2}$ irradiation for an optimized multilayer PSCs [37]. *W. Huang et al.* have also outlined that $E_g$ of BFCO can be tuned from 1.4 eV to 2.1 eV, by controlling Fe/Cr cationic order, and mentioned a polarization of 55μC.cm$^{-2}$, a light absorption coefficient (α) of 2.0E5cm$^{-1}$ and an effective electron−hole pair separation in BFCO thin films [38]. The same group have also reported an increased light absorption coefficient of α=2.5E+5 cm$^{-1}$ at 520 nm for BFCO [30]. In a recent work [39], a bandgap tuning was theoretically achieved by partial substitution of bismuth with lanthanum in highly distorted BFCO (PNMA structure), herein, a promising bandgap of $E_g$=1.54 eV has been demonstrated for $(La_{0.5}Bi_{0.5})_2FCO$ (with light absorption spectrum ~805 nm, red-shifted compared to BFCO), La/Bi substitution heavily engineers the band structure, and strongly impacts the optical properties, however, the light absorption coefficient has been negatively impacted. A promising theoretical PCE of 23.87% has been predicted by *A. Raj* et al. for La-doped BFO (BLFO) solar cells, highlighting the material's potential for further optimizations [40]. The same group have combined experimental and theoretical investigations of La and Ti-doped $BiFeO_3$ (BLFTO) and revealed PCE of ~5.61% for a FTO/$TiO_2$/BFO/Spiro-OMeTAD/Au heterostructure device [41]. In this study, an all-inorganic PSC exploiting BFCO absorber layer is investigated then optimized by employing the SCAPS-1D solar cell simulator. First, we started with calibrating the input parameters through comparing our simulation results with experimental data. Two experimental devices in p-i-n and i-n configurations with respective BFCO bandgaps of 1.7/1.8 eV are used to construct the calibration cells. The comparative analysis regarding the experimental devices underscores the need for design enhancement, given the weak PCE. Therefore, following the calibration step, we propose an improved solar cell design in the n-i-p configuration. For the proposed device, we have investigated the impact of the thickness of the BFCO absorber, ETL and HTL on the overall PV performances. After obtaining optimal thicknesses, we have studied the impacts of defects' densities, series and shunt resistances, and the working temperature. The resulting n-i-p PSC showed a superior PCE. The investigation is carried out under 1 sun illumination.

## 2. Simulation parameters

### 2.1. SCAPS-1D

This study solicits the one-dimensional Solar Cell Capacitance Simulator (SCAPS-1D V3.3.10 −10/04/2021). Widely used by the PV research community [42–47], this software has been developed by Pr. Marc Burgelman et al. [48–51] at the Department of Electronics and Information Systems 'ELIS', University of Gent, Belgium. It was originally designed to simulate polycrystalline thin-film solar cells such as: amorphous-Si, CdTe and CIGS, but now its use is well extended to silicon and perovskite solar cells. It is able to simulate solar cells with up to seven layers with three deep levels for each layer. The main PV parameters including open-circuit

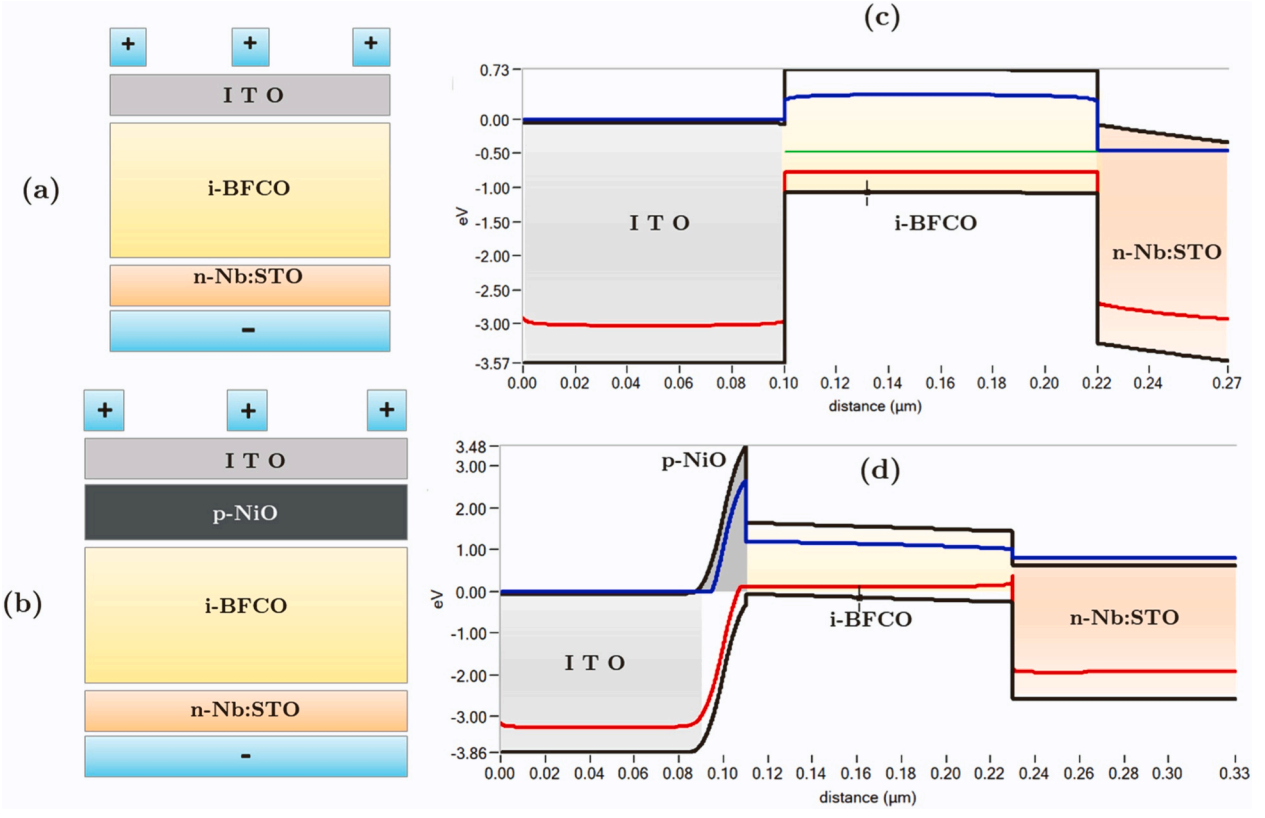



**Fig. 1.** Typical experiment-inspired BFCO-based perovskite solar cells in: (a) i-n and (b) p-i-n configurations. (c) and (d) present the energy band diagrams of the i-n and p-i-n BFCO solar cells.

**Table 1**
Input calibration parameters for the SCAPS-1D model in the i-n (BFCO/Nb:STO) and p-i-n (NiO/BFCO/Nb:STO) configurations as compared with the experimental model in ref [54].

| Parameter | n-ITO [66] | p-NiO [67] | i-BFCO | n-Nb:STO [68] |
|---|---|---|---|---|
| Role | Window | HTL | Intrinsic | ETL |
| Thickness w(nm) | 100 | 50 | 120 [54] | 100 |
| Bandgap energy $E_g$ (eV) | 3.5 | 3 | 1.7/1.8* | 3.2 |
| Electron affinity $\chi$ (eV) | 4.0 | 3.25 | 508 [37] | 4.1 |
| Relative dielectric permittivity $\varepsilon_r$ | 9.0 | 7.12 | 75 [69] | 9.0 |
| Electron mobility $\mu_n$ ($cm^2$/Vs) | 20 | 200 | 4** | 10 |
| Hole mobility $\mu_p$ ($cm^2$/Vs) | 10 | 9 | 3** | 10 |
| CB Effective density of states $N_C$ ($cm^{-3}$) | 2.2E+18 | 2.0E+17 | 4.7E+18** | 5.2E+18 |
| VB Effective density of states $N_V$ ($cm^{-3}$) | 1.8E+18 | 1.1E+19 | 2.4E+18** | 1.0E+18 |
| Electron thermal velocity $\upsilon_e$ (cm/s) | $10^7$ | $10^7$ | 1.3E+16** | $10^7$ |
| Hole thermal velocity $\upsilon_h$ (cm/s) | $10^7$ | $10^7$ | 2.3E+16** | $10^7$ |
| Acceptor density $N_A$ ($cm^{-3}$) | - | $10^{19}$ | $10^6$ | - |
| Donor density $N_D$ ($cm^{-3}$) | $10^{16}$ | - | $10^6$ | $10^{16}$ |
| Defects density $N_t$ ($cm^{-3}$) | $10^{14}$ | $10^{14}$ | $10^{16}$ | $10^{14}$ |

* $E_g$=1.7 eV for the i-n device (#2) and 1.8 eV for the p-i-n device (#4).
** Our calculations (see Section 2.3).

**Table 2**
Solar cell's parameters set in the simulation.

| | |
|---|---|
| Series resistance $R_s$ ($\Omega.cm^2$) [54] | 25 |
| Shunt resistance $R_{sh}$ ($\Omega.cm^2$) [54] | 323 |

voltage ($V_{OC}$), short circuit current density ($J_{SC}$), fill factor (FF), external quantum efficiency (EQE%), and power conversion efficiency (PCE), generation and recombination profiles, heterojunction energy band structure, etc. All these measurements can be calculated and obtained in dark and light conditions at different temperatures and illuminations. Recombination in deep bulk levels and their occupation is described by means of the Shockley-Read-Hall formalism (SRH), while, recombination at the interface states is described by an extension of the SRH formalism. The working principle of SCAPS-1D is based on solving basic semi-conductor equations including the Poisson's equations for electrons and holes, the continuity equations for electrons and holes and the carrier transport equations for electrons and holes in one dimensional approach that are detailed elsewhere [47,52,53]. One strong point in SCAPS-1D is the batch feature, this option let you simulate the effect of many internal and external parameters at a chosen range for a selected number of steps all simultaneously, this allowed us to optimize our study and obtain high quality plots and data.

### 2.2. Materials parameters and device configurations

In this research, the lead-free bismuth-based multiferroic $Bi_2FeCrO_6$ (BFCO) DP is used as the active absorbing layer. Although not yet in a mature stage, the first BFCO-based PSCs have demonstrated interesting PV features that we intend to investigate and enhance further. BFCO crystallizes in the centrosymmetric orthorhombic space group PNMA (No.62). In the unit cell, Bi atoms occupy the perovskite 4c site, O atoms occupy the 4c and 8d positions while the Cr/Fe atoms occupy the 4b positions (Wyckoff notation). *Huang et al.* [54] fabricated the first BFCO-based PV devices in i-n and p-i-n configurations. In those devices, BFCO perovskite has been used as an intrinsic absorber, where, in the i-n device, it was grown over a n-type Nb-doped strontium titanate Nb:$SrTiO_3$ (NSTO) substrate to form the heterojunction. Whereas, in the p-i-n device, it is sandwiched between a p-type NiO and n-type NSTO. The real p–i–n device yielded, under 1 sun illumination and at ambient temperature, a short-circuit current density ($J_{SC}$) of 8.0 mA/$cm^2$, a $V_{OC}$ of 0.53 V, a fill factor (FF) of 48% and a PCE of 2.0%, that is a four-fold enhancement compared to the simpler i-n device which yielded 3.3 mA/$cm^2$, 0.42 V, 56% and 0.8% for $J_{SC}$, $V_{OC}$, FF and PCE under the same conditions, respectively [54]. The p-type conductivity in BFCO (just like in $BiFeO_3$ (BFO) [55] and most ferroelectrics [56]), is likely to appear only in the polycrystalline phase, whereas, strongly depending on the growth conditions, epitaxial BFCO and BFO thin films grown with high crystallinity and low defect concentrations showed rather a n-type behavior [55,57]. The ETL material is n-NSTO, while the HTL is p-NiO. STO (NSTO) is highly regarded as a suitable substrate for the growth of perovskite thin films. The Si/STO system is considered an ideal passive prototype which will play an important role in integrating perovskites into conventional silicon-based solar cells [58]. In the case of BFCO, NSTO has been selected as a convenient HTL that allows a small lattice mismatch (~0.64%) promoting almost stress-free thin films [54]. The NiO is a cubic wide bandgap transparent p-type semiconductor with a large bandgap of $E_g$ =3.6 eV, it is usually deposited in the form of very thin layers (10 nm) allowing ~70% of transmittance in the visible range [54]. The calibration solar cells derived from experiment [54] in the typical i-n and p-i-n configurations are shown in Fig. 1(a) and (b) respectively. The full p-i-n device has a structure of ITO/n-NSTO/i-BFCO/p-NiO. The bottom HTL layer of NiO is connected to the external anode via a default metallic contact (which could, for example, be grown over a transparent ITO layer to create a bifacial device). The energy band diagrams for those solar cells are illustrated in Fig. 1(c) and (d). The SCAPS-1D simulation is conducted using the global AM1.5 G (100 mW/$cm^2$) standard illumination spectrum at an operating temperature of 300 K. The simulation parameters for each layer of the solar cell were derived from

**Table 3**
Defects parameters of the BFCO layer used in the simulation.

| Parameter | Defect 1 (BFCO) |
|---|---|
| Charge type | Neutral |
| Total density ($cm^{-3}$) | $1\times10^{18}$ |
| Energetic distribution | Gaussian |
| Energy level (eV) | 0.60 (above EV) |
| Capture cross section ($cm^2$) | $10^{-15}$ |
| Capture cross section holes ($cm^2$) | $10^{-15}$ |
| Electron diffusion length (Ln)(μm) | 8.9E-2 |
| Electron diffusion length (Lp)(μm) | 5.8E-2 |

**Table 4**
Defects parameters of the p-NiO/i-BFCO (IL1) and BFCO/n-Nb:STO (IL2) interfaces.

| Parameter | IL1 | IL2 |
|---|---|---|
| Defect type | Single acceptor (0/−) | Single acceptor (0/−) |
| Energetic distribution | Gaussian | Gaussian |
| Capture cross section ($cm^2$) | $10^{-19}$ | $10^{-19}$ |
| Capture cross section holes ($cm^2$) | $10^{-19}$ | $10^{-19}$ |
| Reference for defect energy level $E_t$ | Above highest $E_v$ | Above highest $E_v$ |
| Total density ($N_t$) ($1/cm^2$) | $10^{17}$ | $10^{22}$ |
| Density at peak energy ($1/cm^2.eV$) | 3.39E+18 | 5.64E+22 |
| Energy with respect to Reference (eV) | 0.6 | 0.6 |
| Characteristic energy (eV) | 0.1 | 0.1 |

literature and are summarized in Table 1. Some missing parameters are calculated in the next subsection. Other initial device parameters, such as series ($R_s$) and shunt resistance ($R_{sh}$) are listed in Table 2. The bulk defects within the BFCO absorber are indicated in Table 3. The density of defects was evaluated in relation to the interface layers of NiO/BFCO and BFCO/NSTO. The defect parameters at these two interfaces are almost the same except the total defect density $N_t$ which was slightly tuned. Defects of ETL and HTL layers were taken as neutral, and their energetic distribution was modeled using a Gaussian distribution with a characteristic energy of 0.1 eV and a trap defect density of 1.0+E12$cm^{-2}$. The other defect factors are presented in Table 4.

### 2.3. Calculating the missing parameters

The performance of a PV device strongly depends on charge carriers' densities, life time of photogenerated carriers, and their mobilities, presence of grain boundaries, different defects, dislocations etc. [56,59]. *Yi-Fan et.al* showed that, for a perovskite solar cell, the optimal mobilities values of the HTL and the perovskite layer are influenced by both doping concentrations and layer thicknesses [60]. To the best of our knowledge, no data is available on electron and hole mobilities of the BFCO perovskite, therefore, we will have to calculate them. Several mobility models (MMs) can be used to estimate electron and hole mobilities for a given material. Among them we cite: the Arora (AMM), the power law (PLMM), the Boltzmann transport (BTMM), the Fletcher (FMM), the Lombardi surface (LSMM), and the Caughey-Thomas (CTMM). All these models have similar approaches and use empirical data as inputs. In this simulation, we choose to proceed with the CTMM model explained hereafter. Within this approach, electron and hole mobilities are calculated as functions of doping levels using the following expression [61,62]:

$$\mu_{e,h}(N) = \mu_{e,h_{min}} + \frac{\mu_{e,h_{max}} - \mu_{e,h_{min}}}{1 + (N/N_{ref})^{\alpha}} \quad (1)$$

Where: $\mu_{e,h}$ is electron/hole mobility and N is the corresponding total doping concentration ($N_D$ or $N_A$ respectively). $\mu_{max}$, $\mu_{min}$, $N_{ref}$, and α are the temperature-dependent fit parameters, they are usually extracted from fitting experimental measurements of carriers' mobilities as functions of temperature and they depend on the type of the studied material, they represent: the maximal and the minimal electron/hole mobilities, and the reference doping concentration (taken as $N_{ref}=10^{14}$ $cm^{-3}$) respectively. As aforementioned. The large effective mass of electrons reduces their mobility, and limits their contribution to the photocurrent. Generally, the mobility of electrons in FE material is much lower than in silicon for example (~1500 $cm^2V^{-1}s^{-1}$) and typically lies in the range of 0.1–3.0 $cm^2V^{-1}s^{-1}$ [56], though it can be increased to 100 $cm^2V^{-1}s^{-1}$ in La-doped Pb(Zr,Ti)$O_3$ (PLZT) [56], and could reach values as high as $10^4$ $cm^2V^{-1}s^{-1}$ in Co-doped (La,Sr)$TiO^3$ thin films [63]. Effective masses for electrons and holes in BFCO $m_e$* and $m_h$* are: $m_e$*=8.2 $m_0$ and $m_h$*=2.5 $m_0$. ($m_0$ is the initial electron mass $m_0$=9.1E-31 Kg) [64]. We expect carriers' mobilities in BFCO to be low as it has higher effective masses for charge carriers. We took: $\mu_{e\text{-}min}$=0.1 $cm^2V^{-1}s^{-1}$ and $\mu_{e\text{-}max}$=3 $cm^2V^{-1}s^{-1}$. We take value for the BFO material as: $\mu_{h\text{-}min}$=1 $cm^2V^{-1}s^{-1}$ and $\mu_{h\text{-}max}$=5 $cm^2V^{-1}s^{-1}$. Dimensionless α is taken as α=1. We estimate mobilities as: $\mu_e$~3 $cm^2V^{-1}s^{-1}$ and $\mu_h$~4 $cm^2V^{-1}s^{-1}$. The low electron and hole mobilities of BFCO restrain the charge collection and therefore lead to lower PV performances. BFCO, despite tending towards a n-type behavior, is used as an intrinsic layer, the concentration of donors and acceptors should be equal or close, therefore, we took initial values as N=$N_A$=$N_D$=$10^9$ $cm^{-3}$. We have also calculated the

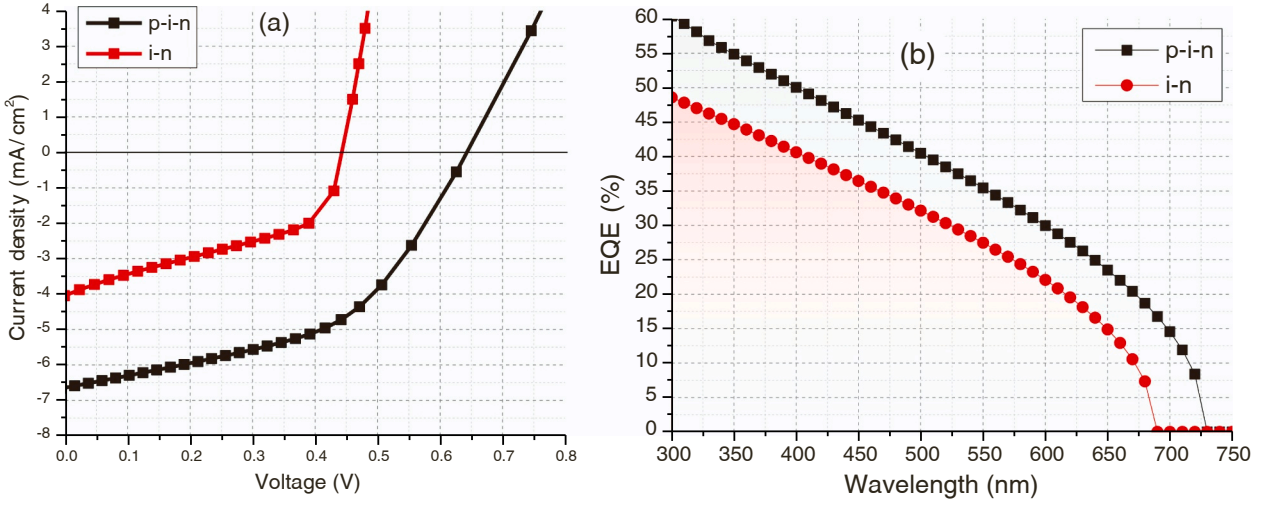



**Fig. 2.** Calibration of initial simulation parameters through (a) J-V characteristic and (b) EQE spectrum of the BFCO-based solar cells in the i-n and p-i-n configuration both built according to similar experimental models from [54].

**Table 5**
Main PV parameters and relative error between SCAPS-1D simulation results and measurements.

| Structure | Results | PV parameters | | | |
|---|---|---|---|---|---|
| | | $J_{SC}$ (mA/cm$^2$) | $V_{OC}$ (mV) | FF (%) | PCE (%) |
| i-n | Simulation | 4.0 | 0.41 | 49.8 | 0.82 |
| | Measured [54] | 3.3 | 0.42 | 56 | 0.8 |
| | Relative error Δζ | 21% | 2.38% | 11% | 2.5% |
| p-i-n | Simulation | 8.4 | 0.55 | 43.6 | 2.02 |
| | Measured [54] | 7.97 | 0.53 | 48 | 2 |
| | Relative error Δζ | 5.4% | 3.77% | 9.16% | 1% |

conduction and valence effective density of states ($N_c$ and $N_V$) for the BFCO layer, using the following formulae:

$$N_C = 2\left(\frac{2\pi.m_e^*.k_BT}{h^2}\right)^{3/2}, N_V = 2\left(\frac{2\pi.m_h^*.k_BT}{h^2}\right)^{3/2} \quad (2)$$

Where: $m_e$* ($m_h$*) denote the electron (hole) effective masses, respectively. $k_B$ is the Boltzmann constant ($k_B$=1.38E-23 m$^2$Kgs$^{-2}$K$^{-1}$), T is the ambient room temperature (T=300 K), and $h$ is the Plank's constant ($h$=6.62E-34 m$^2$Kgs$^{-1}$). Through Eq. (2) the conduction and valence effective density of states for BFCO are found as $N_C$=4.7E+18 cm$^{-3}$ and $N_V$=2.4E+18 cm$^{-3}$. Similarly, we have also calculated the electron and hole thermal velocities as follows:

$$\upsilon_e = \sqrt{\frac{3k_BT}{m_e^*}}, \upsilon_h = \sqrt{\frac{3k_BT}{m_h^*}} \quad (3)$$

The capture cross section for electrons and holes are calculated using the following formulae [65]:

$$\sigma_e = \frac{1}{N_t \quad \tau_c \quad \upsilon_e}, \sigma_h = \frac{1}{N_t \quad \tau_c \quad \upsilon_h} \quad (4)$$

Where: $N_t$ represents the density of trapping centers (defects), $\tau_c$ is the trapping lifetime, and $\upsilon_e$ ($\upsilon_h$) are the thermal velocity of electrons (holes). Using Eq. (3) we define the electron and hole thermal velocities as $\upsilon_e$=1.3E+6 cm.s$^{-1}$and $\upsilon_h$=2.3E+6 cm.s$^{-1}$. The trapping lifetime of carriers in BFCO has not been found in literature, therefore, we cannot calculate the capture cross sections for charge carriers.

## 3. Results and discussions

### 3.1. Calibration of simulation parameters

In order to validate simulation parameters, we have simulated PSCs in both i-n and p-i-n configurations inspired from experimental devices consisting of a BFCO intrinsic absorber layer [54]. The experimental PV parameters are reported as: $J_{SC}$=3.3 mA/cm$^2$, $V_{OC}$=0.42 V, FF=56%, PCE=0.8%, and 7.97 mA/cm$^2$, 0.53 V 48%, 2% for the experimental device named #2 (i-n) and#4 (p-i-n) respectively [54]. Our SCAPS-1D results, tracked via J-V and EQE curves, are illustrated in Fig. 2(a) and (b), and the main PV parameters are listed in Table 5 in comparison with experimental results. It can be noticed that, for the i-n solar cell, $J_{SC}$ is slightly higher and FF is lower, while the $V_{OC}$ and PCE are in good agreement with experiment. Whereas, for the p-i-n cell, the $J_{SC}$ is slightly lower and $V_{OC}$ is higher, FF and PCE are in a fair agreement with the measured values. The differences in $J_{SC}$ and $V_{OC}$ arise from the missing physical parameters needed for SCAPS-1D simulation that we have calculated. In Fig. 2(a), the J-V characteristic for the p-i-n cell shows an increasing in PV parameters except the FF which has decreased comparing to the i-n cell. The significant increase in current density in the p-i-n device, which is affected by the photo-generated minority-carrier currents, is due to the additional p-NiO layer that contributes via its excited photo-generated carriers beside the BFCO ones, in addition to the increased driving force provided by the internal electric field, both endorsed by the depletion regions formed at the p-i and i-n interfaces in the p-i-n device [54]. In Table 5, rows indicating the relative errors between experimental and simulated data are added. This error is a measure of precision that indicates the divergence and accuracy of the simulation and could be a good indicator to its reliability. It is calculated as: Δζ= |simulated-measured|/measured. Among 8 PV parameters, 7 of them have errors below 10%, except in the *n-i* cell, in which the error in FF is 11% and reaches 21% in $J_{SC}$, this has been regulated in the *p-i-n* model which will be used in the coming steps of optimization. To elucidate the enhancement in $J_{SC}$, the external quantum efficiency (EQE) of the i-n and p-i-n cells was simulated for the wavelength range of 300–850 nm under AM1.5 G illumination, and are illustrated in Fig. 2(b). Contrasting the experiment, which exhibited low EQE curves with maximum peaks of 12% at 560 nm and 32% at 650 nm for the i-n and p-i-n cells respectively [54], this low response is probably due to some limitations regarding ITO which is not included in the first calibration simulation due to the known 'convergence-failure' problem in SCAPS-1D that arises when ITO (n-type) is added on top of the p-NiO HTL. Adding ITO layer, if needed, will be rather on top of a HTL (n-Nb:STO) in an n-i-p cell. The simulated EQE of both i-n and p-i-n cells, shows their capabilities of absorbing a wider range of the spectra, particularly in the visible region, owing to their adapted bandgaps. It can be seen from Fig. 2(b), that EQE is maximal at 300 nm, marking 50% for i-n and 60% for the p-i-n device, then it takes a downward trend to about 700 nm in

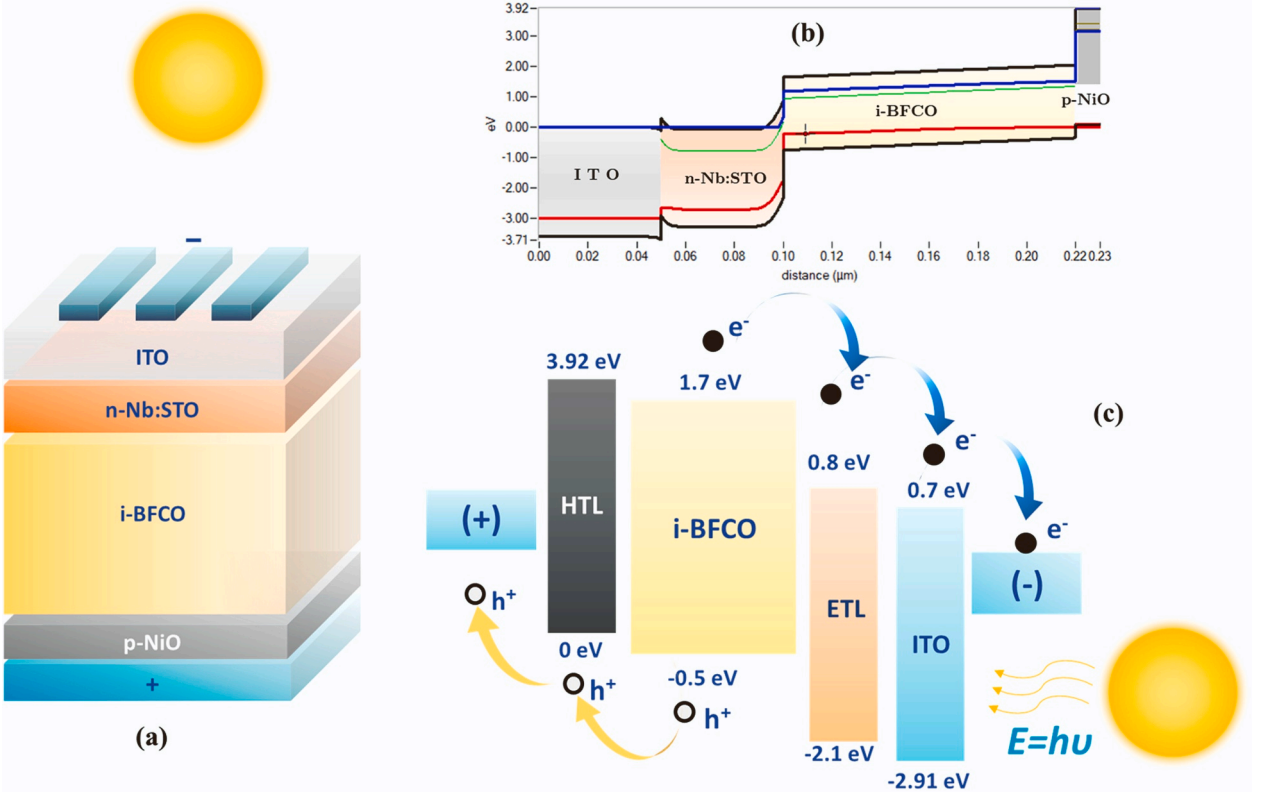



**Fig. 3.** Structure of the proposed BFCO-based perovskite solar cell: (a) schematic of the n-i-p configuration, (b) the energy band diagram from SCAPS-1D and (c) the energy level diagram.

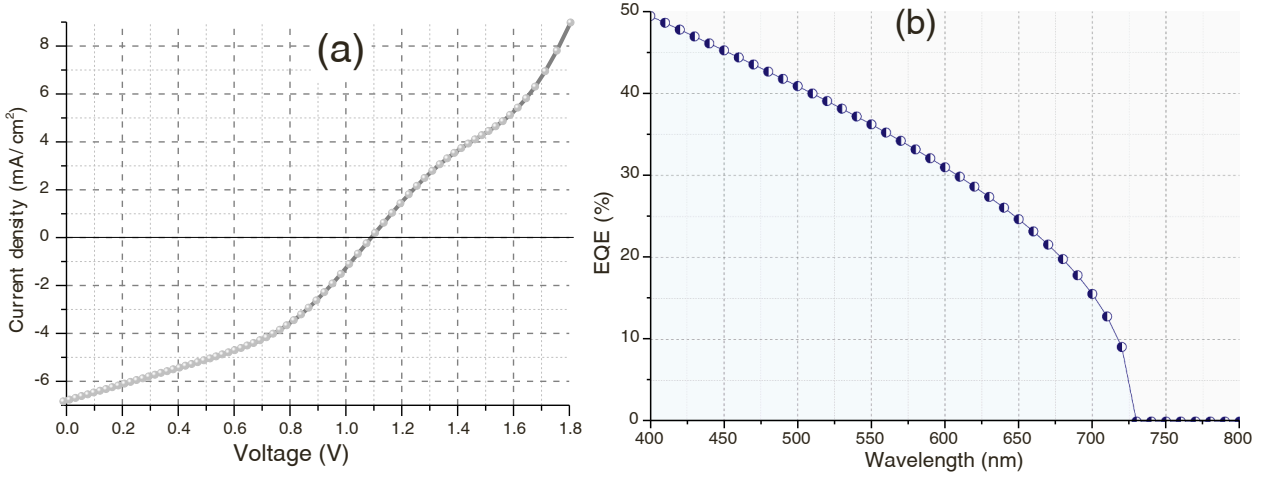



**Fig. 4.** Initial PV performances of the BFCO-based solar cell in the proposed n-i-p configuration tracked via (a) the J-V characteristic and (b) the EQE curve.

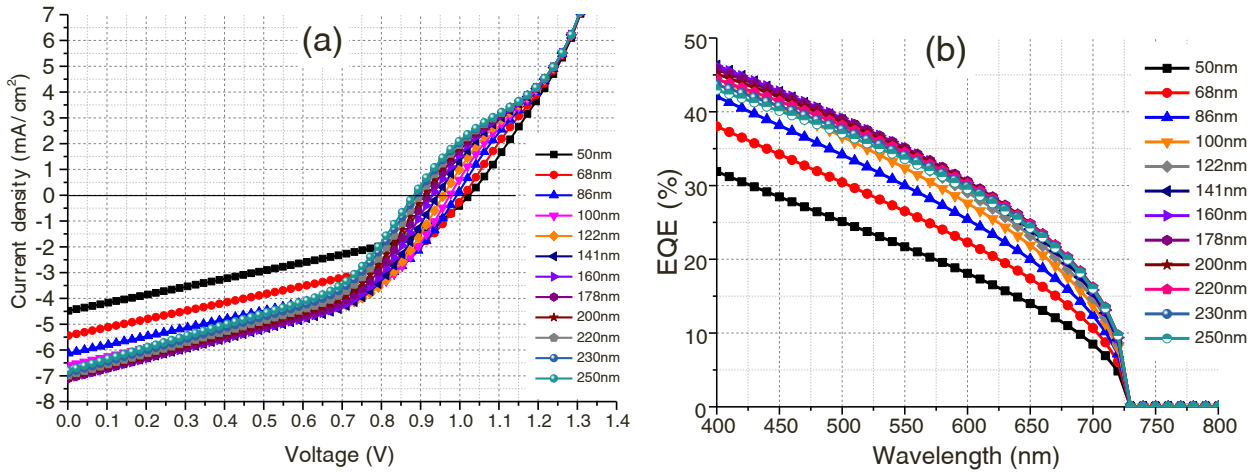



**Fig. 5.** Influence of the thickness of the BFCO layer (in the range 50–250 nm) on (a) the J-V characteristic and (b) EQE of the n-i-p BFCO PSC.

both cases. This Shows that BFCO has a favorable bandgap energy capable of absorbing photons until the wavelength of about 700 nm. The EQE spectrum does not exhibit any absorption beyond 690 nm and 735 nm for i-n and p-i-n respectively. The enhanced EQE spectrum of the p-i-n is related to its higher $J_{SC}$ that results from the extra photocurrent delivered by the p-type NiO. It's worth mentioning that matching experimental results using calculated input parameters is somehow challenging, however, through many simulations, we believe that the obtained calibration parameters are now ready to be carried and optimized in what follows.

### 3.2. Simulation of n-i-p BFCO solar cell

Following the calibration step, we now conduct a n-i-p solar cell simulation with a full structure of ITO/n-NSTO/i-BFCO/p-NiO. The same material and defect parameters, as well as resistances, are kept across all the layers and their respective interfaces. The energy band diagram after contact demonstrates an enhanced alignment comparing to the p-i-n device, in the latter, a n-type ITO layer [70] on the p-NiO creates an additional p-n heterojunction that brings its built-in electrical field which blocks the charge carriers flow, thus, negatively impacts the PV performance. Inverting the structure allows a smoother carrier transport without potential barriers. However, the choice of ETL and HTL with low band misalignment could be further investigated for BFCO-based PSCs. Fig. 3(a) illustrates the adopted n-i-p cell structure. Fig. 3(b) and (c) show the energy band diagram and the energy level diagram respectively. The obtained J-V characteristic for the n-i-p solar cell with ITO layer is illustrated in Fig. 4(a) along with the EQE (Fig. 4(b)). After the first simulation, we obtained $J_{SC}$, $V_{CO}$, FF and PCE as 6.80 mA/cm$^2$, 1.1 V, 40.12% and 2.98%, respectively. It can be seen that $J_{SC}$ is decreased regarding the experimental p-i-n device (7.97 mA/cm$^2$), while $V_{OC}$ is almost doubled (0.53 V). FF slightly decreased from 48% to 40.12%, whereas, PCE is enhanced by 49% from 2% (experimental p-i-n) to 2.98% in our n-i-p device. This indicates that the inverted n-i-p structure we suggest here is more efficient, nevertheless, it still needs more improvements to compete.

The main feature of the obtained J-V characteristics (under illumination), indicated in Fig. 4(a), presents a peculiar concave shape within the fourth (power generating) quadrant, instead of exhibiting the normally expected, so-called "J-shaped" type conventional convex shape. This deformation is commonly referred to as the "S-shaped" J-V characteristic. The S-shaped J-V curve, noticed in our simulations, is a matter of continuing research and is frequently observed in p-i-n structures, and also in some configurations in silicon heterojunction solar cells, CdTe, CIGS, a-Si, and even in perovskite and organic solar cells, and are rarely reported in 2D-PSCs [71,72]. It has been suggested that these S-shape "kink effect" of the illuminated J-V curves were linked to a variety of possible effects such as mismatch between the energy levels of the absorber layer and charge transport layers, leading to a barrier for charge extraction [73]. These barriers are usually created through the large mismatch in energy band alignment between the BFCO absorber ($E_g$=1.7/1.8 eV) and the HTL($E_g$=3.82 eV) on one hand, and BFCO and ETL($E_g$=3.2 eV) on the other hand (see Fig. 3(b)). Other factors contribute also to these barriers through defects or dipoles at the interfaces, the unbalance of charge carrier mobilities, energy barriers, low surface recombination rates, and interfacial defects leading to increased charge recombination [74]. Although the causes of the S-shape curve may appear quite different, the mechanism is in essence the same, i.e. the carrier accumulation inside the device, which alters the distribution of the built-in electric fields [74]. In our case, the use of $NiO_x$ layer is an additional cause of the S-shaped behavior, *Zhong et al.* found that the J-V curves of the $NiO_x$-based devices exhibit an S-shape around the open-circuit voltage, resulting in a higher $V_{OC}$ value and a relatively lower FF [71]. The presence of such bend seriously reduces the FF by depressing the location of the maximum power point (MPP), and thus represents a serious impairment for the PCE that must be avoided, minimized or suppressed [74–76]. To overcome this issue, many internal and external parameters are necessarily optimized, including, but not only: layers thicknesses, charge carriers mobilities, defect densities, resistances etc. [77–80], in what follows, their influence will be examined. It is worth noting that BFCO, if used in a specific multilayer configuration could obtain higher efficiencies, a record PCE for ferroelectric-based PSC of 8.1% has been recorded by *R. Nechache et al.* [37] using an optimized multilayer configuration in which the bandgap of each BFCO layer is finely controlled by changing the deposition rates. This type of promising solar cells could be covered in another

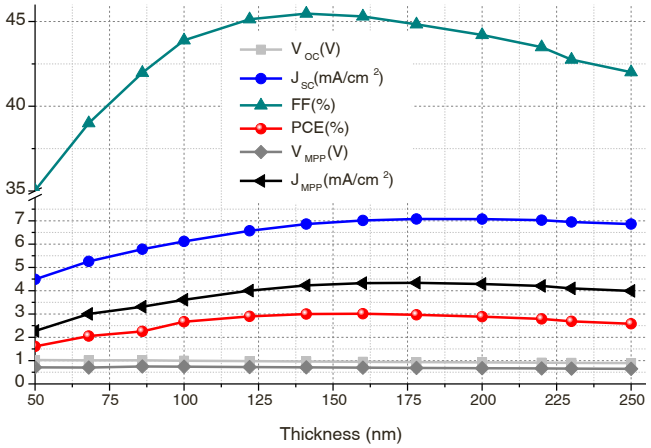



**Fig. 6.** Variation of the n-i-p device performance with BFCO absorber thickness layer in the range 50–250 nm.

investigation. External quantum efficiency for the proposed n-i-p solar cell illustrated in Fig. 4(b) shows a better response to the AM1.5 G illumination, herein, a maximum peak of ~68% at 350 nm, with a broader absorption spectrum regarding the p-i-n experimental configuration. This enhancement of EQE is directly related to the improvement of the light absorption through the increasing of photocurrents and $J_{SC}$.

### 3.3. *Effect of the thickness of BFCO perovskite*

In general, perovskites exhibit direct bandgaps, higher light absorption coefficients and charge carrier diffusion lengths normally greater than their thicknesses, allowing most of the photo-generated carriers to reach their respective charge transport layers and/or electrodes, therefore, a thin absorber would be sufficient to achieve acceptable PCEs. Nevertheless, an optimal thickness would be benefic for more light absorption and more release of charge carriers, hence further enhancement of $J_{SC}$ could be achieved. However, if the thickness is too small, the absorption rates will be lower, resulting in reduced photocurrents and decreased efficiencies. On the other hand, if it's too increased, charge carriers may not have sufficient diffusion lengths to reach the charge collecting layers, resulting in higher series resistances hence poor performances, thus, it must be carefully optimized [56,59]. At this phase, the effect of BFCO thickness is assessed using the batch feature of SCAPS-1D. Thicknesses of p-NiO and n-Nb:STO layers were fixed at their default values of 50 nm and 100 nm, respectively. The thickness of BFCO was then varied from 50 nm to 250 nm in 10 steps. J-V curves were plotted in Fig. 5(a). It can be observed that, as the thickness is increased, $J_{SC}$ increases from approximately 4.5 mA/cm$^2$ at 50 nm reaching a maximum of 8 mA/cm$^2$ at 178 nm of BFCO, then slightly decreases to 7 mA.cm$^{-2}$ for 250 nm. This improvement in $J_{SC}$ is caused by the generation of carriers in larger quantities. In contrary, $V_{OC}$ is negatively affected, where it slightly decreases from 1.05 V at 50 nm to 0.89 V at 250 nm of BFCO thickness. The impact of the thickness of BFCO on EQE in the n-i-p cell is illustrated in Fig. 5(b), the wavelength range is between 400 nm to 800 nm. EQE is highly related to the bandgaps of the layers, especially the absorber, BFCO has a bandgap $E_g$= 1.7 eV/1.8 eV, which is not an ideal value for absorbing in the visible range, however, this can be solved through bandgap engineering. For all thicknesses, the peak EQE is found at 400 nm wavelength with negligible absorption beyond 750 nm. For the lowest absorber thickness (50 nm), peak EQE is 32%. It can be observed that EQE positively increases with thickness of BFCO until 141 nm peaking 46.5%, then starts to decline until reaching 43% for 250 nm thickness. However, the EQE does not fully reflect the evolution of the overall photovoltaic performances as the other parameters are strongly reduced by the recombination phenomena in the absorbing layer. The evolution of the four PV parameters with BFCO thickness is traced in Fig. 6. Apparently, PCE increases from 1.55% for 50 nm to a maximum of 3.2% for 160 nm thickness. After this thickness, PCE slightly decreases until reaching 2.5% at 250 nm. Naturally. FF, $J_{SC}$ and $J_{MPP}$ follow the same behavior. The fill factor decreases from 55% to about 43%. We conclude that an ideal BFCO thickness is estimated to be between 140 nm and 180 nm, and we adopt 160 nm as the optimized thickness to be used in next simulation steps. This value would not face experimental challenges as it's relatively close to the experimental one (120 nm [54]).

### 3.4. *Effects of dopants and defects densities of BFCO*

The thickness of the BFCO perovskite is fixed at 160 nm, now, the concentration of donors and acceptors in this layer are equally changed as the materials is intrinsic. Values from N=$N_A$=$N_D$= $10^4$ cm$^{-3}$ to $10^{19}$ cm$^{-3}$ are simulated in 10 steps. The batch feature of SCAPS-1D is used again for this simulation. We have noticed that changing $N_A$ and $N_D$ simultaneously have no significant effect, however, if we fix one and vary the other, this will alter the conductivity type and changes the type of the solar cell which is not our goal. The effect of the total defects density ($N_t$) of BFCO has been simulated as well, $N_t$ has been changed from $10^{12}$ cm$^{-3}$ to $10^{18}$ cm$^{-3}$, while $N_A$ and $N_D$ are kept at $10^6$ cm$^{-3}$ and BFCO thickness at 180 nm. Unlike $N_D$ and $N_A$, $N_t$ has a significant impact on the performances of the solar cell, Fig. 7(a) shows the evolution of the J-V characteristic with $N_t$. Our simulation shows that the PV performances are negatively affected by increasing $N_t$, we observe from Fig. 7(a) that $J_{SC}$ as well as $V_{OC}$ are well increased for $N_t$=$10^{12}$ cm$^{-3}$, where,

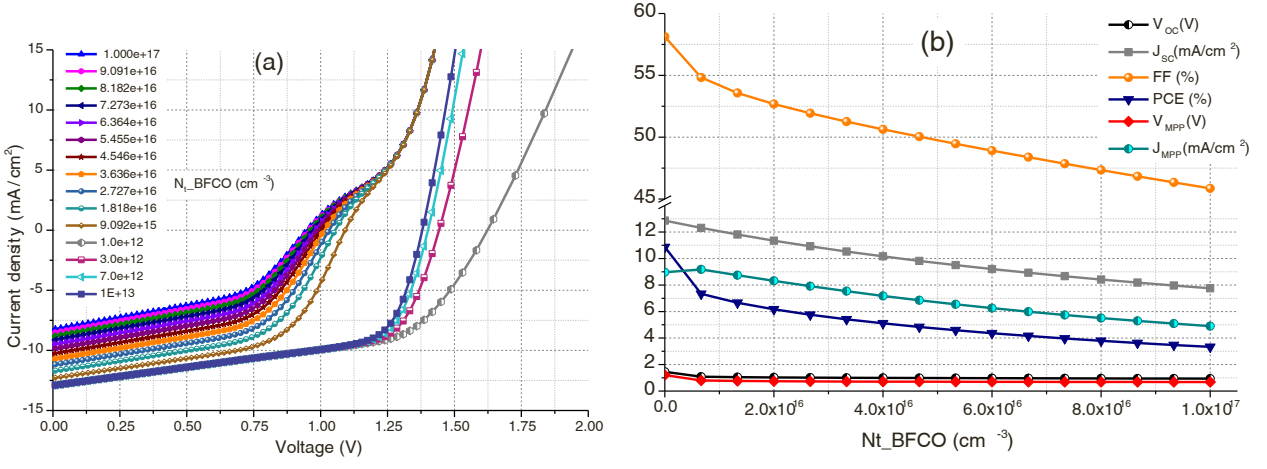



**Fig. 7.** Effect of defect densities of the BFCO layer on (a) the J-V characteristic and (b) main PV parameters.

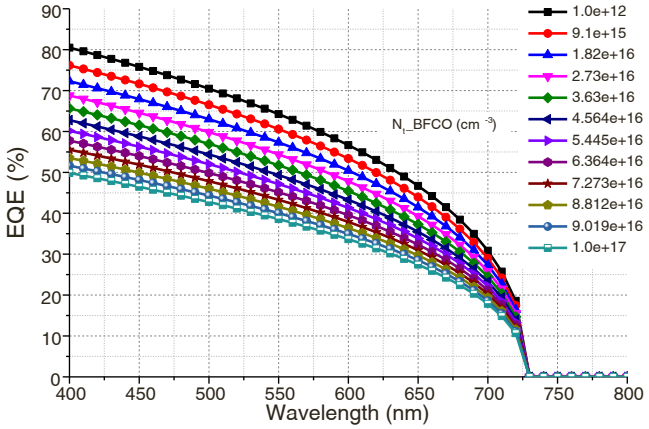



**Fig. 8.** Effect of defect densities of the BFCO layer on the EQE.

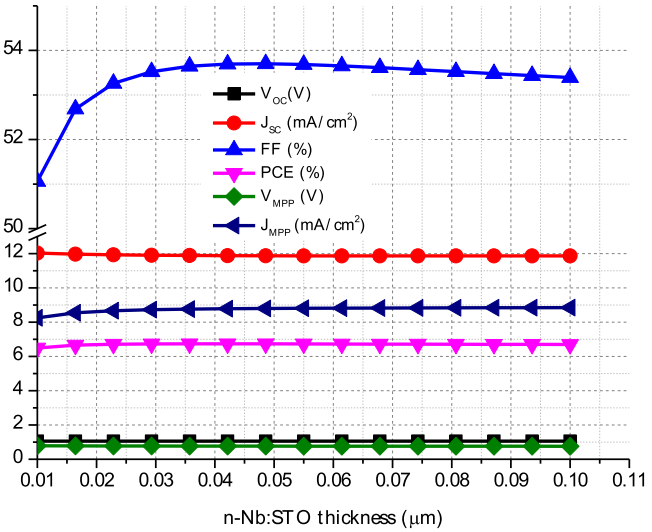



**Fig. 9.** Effect of the thickness of the Nb:STO (ETL) layer on the main PV parameters.

$J_{SC}$ records 13 mA/cm$^2$, while $V_{OC}$ marks 1.62 V, at this value, the s-shape vanished and a well J-shaped J-V curve is obtained, showing the efficiency of our suggested cell configuration (FF reaches 54%, whereas PCE peaks 10.9%). This is the best PV performance recorded so far. Fig. 7(b) illustrates the evolution of PV parameters with $N_t$_BFCO. When moving from $N_t$=$10^{12}$ cm$^{-3}$ to $N_t$=2E+13 cm$^{-3,\ \text{then onwards until}}$ $10^{17}$, PCE drops from 10.9% to 7–3.2%. The fill factor is the most sensitive output to $N_t$ variation, maximal FF of around 58.2% is obtained at $N_t$=$10^{12}$ cm$^{-3}$ and drops to 46% for $N_t$=$10^{17}$ cm$^{-3}$. $V_{OC}$ and $J_{SC}$ are indeed affected as can be seen in the figure. The initial value of $N_t$ at the beginning of this work was tuned at an average value of 1.25E+17 cm $^{-3}$ which is relatively high but could be reasonable in BFCO. While a thicker BFCO absorbs more photons hence more carriers could be generated, these pairs may be recombined easily in such layer with high $N_t$, therefore, a decrement in FF, usually following $J_{SC}$ and affected by $V_{OC}$, is mainly due to internal recombination inside BFCO, arising from short carriers' lifetime. Reducing defects in the perovskite absorber layer comes from optimizing fabrication recipes and is strongly affected by the quality, purity, and crystallinity of its thin films or crystals. Also, the BFCO/NiO and BFCO/Nb:STO interfaces are sources of many defects and carriers' recombination, these should be carefully optimized during the fabrication. A balanced value of $N_t$=2E+16 cm$^{-3}$ at which PCE=6.2% is optimal for our case and is adopted forward. Fig. 8 illustrates the effect of $N_t$_BFCO on EQE. Here is noticed that EQE is as well negatively affected by increasing Nt, it reaches a maximum of 82% at 400 nm, while, for the chosen $N_t$=2E+16 cm$^{-3}$, EQE is ~73%.

### *3.5. Effects of the thickness of the HTL and ETL layers*

In this part, we simulated the effect of thicknesses of the ETL (Nb:STO) and HTL (NiO) layers.

As crucial for PSCs, HTL and ETL could drastically impact the device efficiency and its stability. NSTO layer thickness have a slight effect on the PV performances of the solar cell, the ideal thickness is around 50 nm, the window layer should be thinner to reduce the

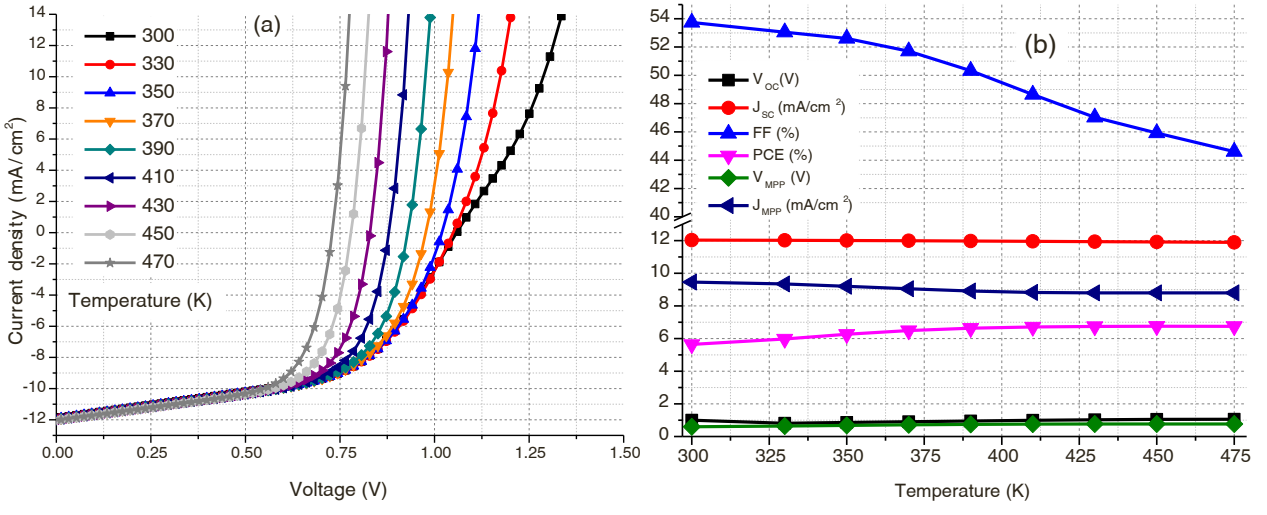



**Fig. 10.** Effect of temperature on (a) JV characteristic and (b) the main PV parameters of BFCO solar cell.

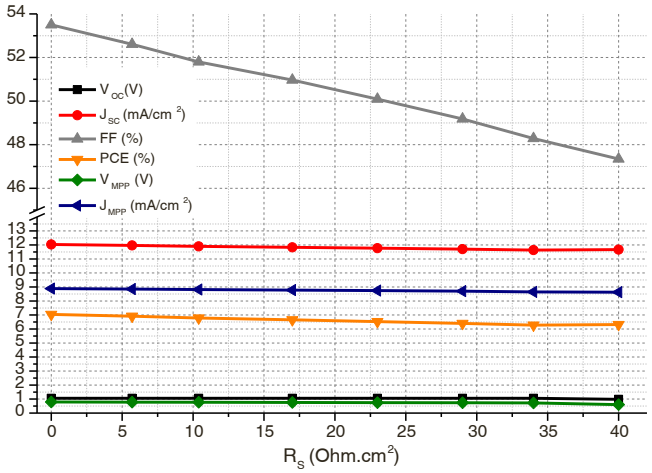



**Fig. 11.** Effect of series resistance $R_S$ on the main PV parameters of BFCO solar cell.

**Table 6**
Optimal configuration of the suggested n-i-p BFCO-based PSC along with its PV performances.

| Configuration | ITO/n-Nb:STO/i-BFCO/p-NiO | | | | |
|---|---|---|---|---|---|
| layers | Thickness (nm) | | $N_t$ ($cm^{-3}$) | $N_A$ ($cm^{-3}$) | $N_D$ ($cm^{-3}$) |
| Nb-STO | 50 | | $10^{14}$ | 0 | $10^{16}$ |
| BFCO | 150 | | $10^{12}$-$10^{16}$ | - | - |
| NiO | 100 | | $10^{14}$ | $10^{16}$ | 0 |
| Parameter | Optimal Value | | | | |
| $R_S$($\Omega.cm^2$) | 5–10 | | | | |
| $R_{SH}$($\Omega.cm^2$) | ~K$\Omega.cm^2$ | | | | |
| T(K) | 275–300 | | | | |
| PV Performance | | | | | |
| Output parameter | $J_{SC}$(mA/$cm^2$) | $V_{OC}$(V) | | FF(%) | PCE(%) |
| Optimal value | 12 | 1.2 | | 53.2 | 7.3 |

recombination effects. Fig. 9 shows the effect of NSTO thickness on the J-V characteristic, when thickness varies from 10 nm to 100 nm, $J_{SC}$, $V_{CO}$, FF and PCE, vary from 12 mA/$cm^2$, 1.65 V, 51% and 6.8% to 11.9 mA/$cm^2$, 1.65 V, 53.3% and 6.85% respectively. A maximum efficiency is not much noted but a maximum FF=53.7% is obtained at 50 nm NSTO thickness, half as in the experiment (100 nm). At this optimal thickness, PCE is obtained as 6.8%, $J_{SC}$ is 12 mA/$cm^2$ and $V_{OC}$=1.12 V. It can be clearly seen that thicknesses of HTL had no significant impacts on certain PV parameters but they must be carefully optimized along the BFCO. We have to add that the lack of ETL and HTLs stability due to their improper choice jeopardizes improvements of PSCs [46]. While the ideal ETL layer for BFCO has been so far the NSTO, the HTL NiO can be changed. Diverse HTLs are used for PSCs, including, but not limited to, triphenylamine [81], conjugated polymers [82], DTP derivatives [83], Spiro-OMeTAD [84] (low hole mobility [85]), PEDOT:PSS [86] (charge transport layers of high transparency, low-temperature processing, mechanical stability, excellent flexibility, and low conductivity [87]). A study can be done to investigate the best possible choice.

### 3.6. *Effect of temperature*

Generally, PCS suffer from instability under high temperatures, this limits their efficiency and robustness, therefore, their usage in harsh environments like deserts is hindered. After we optimized thicknesses and defects, we now simulate the effect of temperature on the performances of our n-i-p device. Fig. 10(a) shows the effect of temperature varied from 300 K to 470 K on the J-V characteristic, we notice that T has a negative impact of the PV performances, the room temperature T=273–300 K is ideal for optimal function of the studied PSC. In this simulation, when T goes from 300 K to 470 K(200°C), we noticed that $V_{OC}$ decreased from 1.1 V to 0.7 V, $J_{SC}$ is less affected and is stable around 12 mA.$cm^{-2}$, FF drastically decreased from ~61% to ~53%, while PCE slightly dropped from 6.8% to 6.48% (Fig. 10(b)). We confirm therefore that the ideal working temperature is 300 K and invite more experimental studies on the subject in order to investigate the deterioration of this PSC under such conditions.

### 3.7. *Influence of series resistance*

We have also optimized both series resistance ($R_S$) and shunt resistance ($R_{SH}$). Ideal values of $R_S$ and $R_{SH}$ should be as close to zero

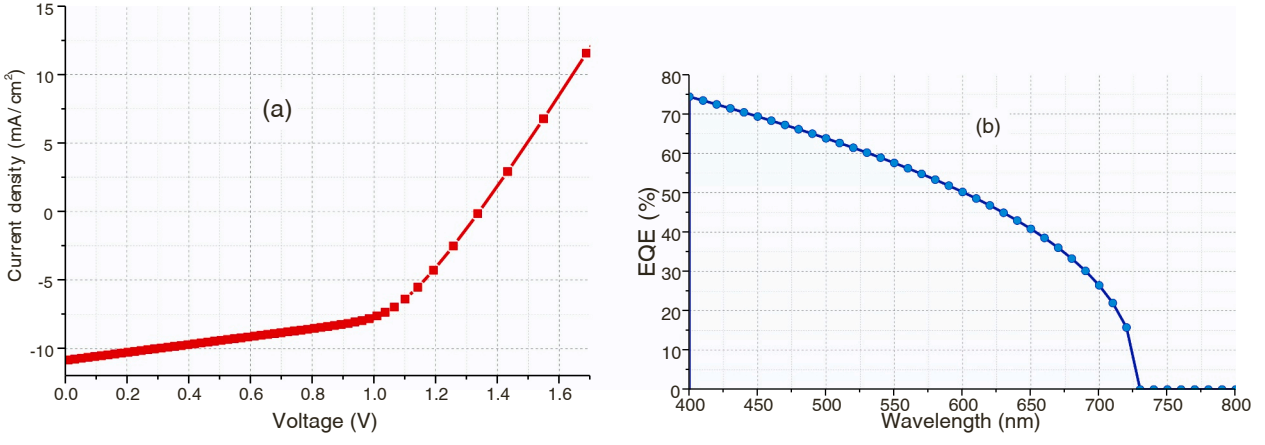



**Fig. 12.** PV output of the final optimized n-i-p BFCO-based PSC through (a) the J-V characteristic, and (b) EQE spectrum.

and as high as possible respectively. Fig. 11 shows the effect of $R_S$ on PV performances. We varied Rs from 0 to 10Ωcm$^2$ (knowing that the initial $R_S$=25 Ωcm$^2$ taken from experiment [54]). It can be noticed that $R_S$ in this narrow range mainly influences FF, whereas other parameters are slightly affected. FF has a maximum value of 53.6% at $R_S$=0Ωcm$^2$ while it drops to 47.3% when $R_S$ reaches 40Ωcm$^2$. Results showed that $R_S$ should be maintained between 10 and 50Ω.cm$^2$ and $R_{SH}$ (experimental value 323 Ω.cm$^2$ [54]) should be around ~KΩ.cm$^2$. Both resistances are affected by the cell design and choice of ETL and HTL materials and the final electrodes. Experimentally, *W. Huang et al.* reported that series resistance for p-i-n BFCO solar cell could be decreased from $R_S$= 57–25Ω.cm$^2$ while $R_{SH}$ could be increased from 269 to 323Ω.cm$^2$ [54], $R_S$ is reasonable in their case, however, $R_{SH}$ is still very low and non-convenient for PV applications.

### 3.8. Final device

The final device we suggest is a n-i-p configuration with ITO/n-Nb:STO/i-BFCO/p-NiO layer structure having the parameters indicated in Table 6, which could, under optimal conditions, generate the PV parameters listed in the same table thereafter. The final J-V and EQE characteristics of the optimizes solar cell are illustrated in Fig. 12(a) and (b). We believe that this kind of solar cells is promising, still in its infancy and need more experimental and theoretical works in order to prove its competitivity in the PV realm.

## 4. Conclusions

In this study, the integration of the double perovskite BFCO into photovoltaics was examined. The simulation parameters were validated through a comparative analysis between i-n and p-i-n structures with their corresponding experimental configurations. Both models had lower conversion efficiencies, therefore, a reconfiguration and further optimizations are engaged in order to increase the PCE. Subsequently, a novel n-i-p structure was introduced. The initial findings for this n-i-p cell, in contrast to the experimental p-i-n model, indicated enhanced performances. Nevertheless, the weak PV performance was observed in both scenarios due to various factors including, -but not only- the thickness of the BFCO layer, its defect concentration, and characteristics of HTL and ETL beside external conditions (temperature) and cell design ($R_s$, $R_{sh}$). Consequently, refining the thicknesses and doping profiles holds potential for further improvement of these outcomes. The optimized n-i-p model we proposed exhibited PCE reaching up to 7.3% when BFCO thickness is at 150 nm and defect density $N_t$ lowered at 2E+16 cm$^{-3}$. While acknowledging the hypothetical nature of these values, which may by experimentally challenging, this model presents a valuable framework for designing future BFCO-based PSCs. Moreover, its applicability extends to its integration with various photovoltaic technologies, including bifacial and tandem solar cells.

## Declaration of Generative AI and AI-assisted technologies in the writing process

During the preparation of this work the author used Google-Bard ai in order to correct some text. After using this tool/service, the author reviewed and edited the content as needed and takes full responsibility for the content of the publication.

## Declaration of Competing Interest

The authors declare that they have no known competing financial interests or personal relationships that could have appeared to influence the work reported in this paper.

## References

[1] H.L. Thadani, Y.I. Go, Large-scale solar system design, optimal sizing and techno-economic-environmental assessment, Sustain. Energy Res. 10 (1) (2023) 11.
[2] S. Rajendra, Why silicon is and will remain the dominant photovoltaic material, J. Nanophotonics 3 (1) (2009) 032503.
[3] H. Soonmin, et al., Overview on different types of solar cells: an update, Appl. Sci. 13 (2023), https://doi.org/10.3390/app13042051.
[4] M. Nakamura, et al., Cd-free Cu(In,Ga)(Se,S)2 thin-film solar cell with record efficiency of 23.35%, IEEE J. Photovolt. 9 (2019).
[5] N. Jayswal, et al., Role of CdTe interface structure on CdS/CdTe photovoltaic device performance, Materials 16 (2023) 6812.
[6] A. Lekhdim, et al., Efficiency improvement of single-junction InGaP solar cells by advanced photovoltaic device modeling, Optik 163 (2018).
[7] E.K. Solak, E. Irmak, Advances in organic photovoltaic cells: a comprehensive review of materials, technologies, and performance, RSC Adv. 13 (18) (2023) 12244–12269.
[8] Z. Bouzid, Y. Halimi, Performance enhancement of eucalyptus extract based dye sensitized solar cell using TiO2/embedded capsaicin photoanode, IEEE Sens. J. 22 (2022) 12761–12768.
[9] Y. Tian, et al.. Advanced Perovskite Solar Cells, 2024, pp. 113–135.
[10] J.-P. Correa-Baena, et al., The rapid evolution of highly efficient perovskite solar cells, Energy Environ. Sci. 10 (3) (2017) 710–727.
[11] K. Deepthi Jayan, V. Sebastian, Comprehensive device modelling and performance analysis of MASnI3 based perovskite solar cells with diverse ETM, HTM and back metal contacts, Sol. Energy 217 (2021) 40–48.
[12] H. Li, et al., Photoferroelectric perovskite solar cells: principles, advances and insights, Nano Today 37 (2021) 101062.
[13] B. Farhadi, et al., Promising perovskite solar cell candidates: enhanced optoelectronic properties of XSrI3 perovskite materials under hydrostatic pressure, Small Struct. n/a (n/a) (2023) 2300328.
[14] A. Soni, K.C. Bhamu, J. Sahariya, Investigating effect of strain on electronic and optical properties of lead free double perovskite Cs2AgInCl6 solar cell compound: a first principle calculation, J. Alloy. Compd. 817 (2020) 152758.
[15] D.-Y. Hu, et al., First-principles calculations to investigate structural, elastic, electronic and optical properties of lead-free perovskite derivatives Cs2SeX6 (X=Cl, Br, I), Opt. Mater. 119 (2021) 111316.
[16] D. Hao, J. Zou, J. Huang, Recent developments in flexible photodetectors based on metal halide perovskite, InfoMat 2 (1) (2020) 139–169.
[17] Q. Dong, et al., Interpenetrating interfaces for efficient perovskite solar cells with high operational stability and mechanical robustness, Nat. Commun. 12 (1) (2021) 973.

[18] Z. Peng, et al., A new perovskite-related ceramic with colossal permittivity and low dielectric loss, J. Eur. Ceram. Soc. 40 (12) (2020) 4010–4015.
[19] Y. Wang, et al., The unique dielectricity of inorganic perovskites toward high-performance triboelectric nanogenerators, Nano Energy 69 (2020) 104418.
[20] Z. Song, et al., A technoeconomic analysis of perovskite solar module manufacturing with low-cost materials and techniques, Energy Environ. Sci. 10 (6) (2017) 1297–1305.
[21] T.M. Brenner, et al., Hybrid organic—inorganic perovskites: low-cost semiconductors with intriguing charge-transport properties, Nat. Rev. Mater. 1 (1) (2016) 15007.
[22] A. Miyata, et al., Direct measurement of the exciton binding energy and effective masses for charge carriers in organic–inorganic tri-halide perovskites, Nat. Phys. 11 (7) (2015) 582–587.
[23] A. Maho, et al., Photonic structuration of hybrid inverse-opal TiO2—perovskite layers for enhanced light absorption in solar cells, ACS Appl. Energy Mater. 4 (2) (2021) 1108–1119.
[24] L.K. Ono, et al., Perovskite solar cells—towards commercialization, ACS Energy Lett. 2 (8) (2017) 1749–1751.
[25] Y. Zhou, Y. Zhao, Chemical stability and instability of inorganic halide perovskites, Energy Environ. Sci. 12 (5) (2019) 1495–1511.
[26] B.-W. Park, et al., Bismuth based hybrid perovskites A3Bi2I9 (A: methylammonium or cesium) for solar cell application, Adv. Mater. 27 (43) (2015) 6806–6813.
[27] T. Miyasaka, et al., Perovskite solar cells: can we go organic-free, lead-free, and dopant-free? Adv. Energy Mater. 10 (13) (2020) 1902500.
[28] H. Chen, et al., Inorganic perovskite solar cells: a rapidly growing field, Sol. RRL 2 (2) (2018) 1700188.
[29] R.E. Brandt, et al., Identifying defect-tolerant semiconductors with high minority-carrier lifetimes: beyond hybrid lead halide perovskites, MRS Commun. 5 (2) (2015) 265–275.
[30] W. Huang, et al., Epitaxial Bi2FeCrO6 multiferroic thin-film photoanodes with ultrathin p-type NiO layers for improved solar water oxidation, ACS Appl. Mater. Interfaces 11 (14) (2019) 13185–13193.
[31] M.V. Rastei, et al., Thickness dependence and strain effects in ferroelectric Bi2FeCrO6 thin films, ACS Appl. Energy Mater. 2 (12) (2019) 8550–8559.
[32] K. Guo, et al., Regulation of photovoltaic response in ZSO-based multiferroic BFCO/BFCNT heterojunction photoelectrodes via magnetization and polarization, ACS Appl. Mater. Interfaces 13 (30) (2021) 35657–35663.
[33] R. Nechache, et al., Photovoltaic properties of Bi2FeCrO6 epitaxial thin films, Appl. Phys. Lett. 98 (20) (2011) 202902.
[34] S. Li, et al., Epitaxial Bi2FeCrO6 multiferroic thin film as a new visible light absorbing photocathode material, Small 11 (32) (2015) 4018–4026.
[35] L. Wei, et al., First-principles investigation of bandgap tailoring in tetragonal Bi2FeCrO6 by magnetic ordering and B-site-cation ordering, Funct. Mater. Lett. 13 (01) (2019) 1950092.
[36] W. Shockley, H.J. Queisser, Detailed balance limit of efficiency of p-n junction solar cells, J. Appl. Phys. 32 (3) (1961) 510–519.
[37] R. Nechache, et al., Bandgap tuning of multiferroic oxide solar cells, Nat. Photonics 9 (1) (2015) 61–67.
[38] W. Huang, et al., Highly sensitive switchable heterojunction photodiode based on epitaxial Bi2FeCrO6 multiferroic thin films, ACS Appl. Mater. Interfaces 10 (15) (2018) 12790–12797.
[39] B. Merabet, et al., Optimal bandgap of double perovskite la-substituted Bi 2 FeCrO 6 for solar cells: an ab initio GGA+ U study, Chin. Phys. Lett. 34 (1) (2017) 016101.
[40] A. Raj, et al., Comparative analysis of 'La' modified BiFeO3-based perovskite solar cell devices for high conversion efficiency, Ceram. Int. 49 (1) (2023) 1317–1327.
[41] A. Raj, et al., Photovoltaic energy conversion in multiferroic perovskite absorber-based devices via experiment and theoretical calculations, Phys. B Condens. Matter 673 (2024) 415504.
[42] M. Belarbi, O. Zeggai, S. Louhibi-Fasla, Numerical study of methylammonium lead iodide perovskite solar cells using SCAPS-1D simulation program, Mater. Today Proc. 51 (2022) 2115–2119.
[43] N.A. Mahammedi, et al., Numerical simulation and optimization of a silicon clathrate-based solar cell n-Si136/p-Si2 using SCAPS-1D program, Opt. Mater. 107 (2020) 110043.
[44] S. Yasin, T. Al Zoubi, M. Moustafa, Design and simulation of high efficiency lead-free heterostructure perovskite solar cell using SCAPS-1D, Optik 229 (2021) 166258.
[45] Q. Chen, et al., The effect of energy level of transport layer on the performance of ambient air prepared perovskite solar cell: a SCAPS-1D simulation study, Crystals 12 (1) (2022).
[46] M.S. Chowdhury, et al., Effect of deep-level defect density of the absorber layer and n/i interface in perovskite solar cells by SCAPS-1D, Results Phys. 16 (2020) 102839.
[47] A. Raj, et al., Investigating the potential of lead-free double perovskite Cs2AgBiBr6 material for solar cell applications: a theoretical study, Int. J. Energy Res. 46 (10) (2022) 13801–13819.
[48] M. Burgelman, P. Nollet, S. Degrave, Modelling polycrystalline semiconductor solar cells, Thin Solid Films 361-362 (2000) 527–532.
[49] K. Decock, P. Zabierowski, M. Burgelman, Modeling metastabilities in chalcopyrite-based thin film solar cells, J. Appl. Phys. 111 (4) (2012) 043703.
[50] J. Marlein, K. Decock, M. Burgelman, Analysis of electrical properties of CIGSSe and Cd-free buffer CIGSSe solar cells, Thin Solid Films 517 (7) (2009) 2353–2356.
[51] M. Burgelman, et al., Advanced electrical simulation of thin film solar cells, Thin Solid Films 535 (2013) 296–301.
[52] A. Morales-Acevedo, N. Hernández-Como, G. Casados-Cruz, Modeling solar cells: a method for improving their efficiency, Mater. Sci. Eng. B 177 (16) (2012) 1430–1435.
[53] H.J. Pauwels, G. Vanhoutte, The influence of interface state and energy barriers on the efficiency of heterojunction solar cells, J. Phys. D Appl. Phys. 11 (5) (1978) 649–667.
[54] W. Huang, et al., Multiferroic Bi2FeCrO6 based p–i–n heterojunction photovoltaic devices, J. Mater. Chem. A 5 (21) (2017) 10355–10364.
[55] J. Song, et al., Domain-engineered BiFeO3 thin-film photoanodes for highly enhanced ferroelectric solar water splitting, Nano Res. 11 (2) (2018) 642–655.
[56] M. A. Jalaja, S. Dutta, Ferroelectrics and multiferroics for next generation photovoltaics, Adv. Mater. Lett. 6 (7) (2015) 568–584.
[57] H. Wei, Transparent Conducting Oxides and Multiferroic Perovskites for Solar Energy Conversion Applications, Université du Québec, Québec: Institut national de la recherche scientifique, Université du Québec,, Québec, 2018, p. 176.
[58] M. Spreitzer, et al., Epitaxial ferroelectric oxides on silicon with perspectives for future device applications, APL Mater. 9 (4) (2021) 040701.
[59] Y.-F. Gu, et al., Effect of carrier mobility on performance of perovskite solar cells, Chin. Phys. B 28 (4) (2019) 048802.
[60] Yi-Fan Gu, H.-J. Du, N.-N. Li, L. Yang, C.-Y. Zhou, Effect of carrier mobility on performance of perovskite solar cells, Chin. Phys. B 28 (4) (2019), p. 48802-048802.
[61] D.M. Caughey, R.E. Thomas, Carrier mobilities in silicon empirically related to doping and field, Proc. IEEE 55 (12) (1967) 2192–2193.
[62] T.T. Mnatsakanov, et al., Carrier mobility model for GaN, Solid-State Electron. 47 (1) (2003) 111–115.
[63] G. Herranz, et al., High-spin polarized Co-doped (La,Sr)TiO3 thin films on high-mobility SrTiO3 substrates, J. Magn. Magn. Mater. 310 (2, Part 3) (2007) 2111–2113.
[64] D. Kim, et al., Electron−hole separation in ferroelectric oxides for efficient photovoltaic responses, Proc. Natl. Acad. Sci. 115 (26) (2018) 6566–6571.
[65] D.C. Hoesterey, G.M. Letson, The trapping of photocarriers in anthracene by anthraquinone, anthrone and naphthacene, J. Phys. Chem. Solids 24 (12) (1963) 1609–1615.
[66] Naureen, et al., A comparative study of quantum dot solar cell with two different ETLs of WS2 and IGZO using SCAPS-1D simulator, Solar 2 (2022) 341–353, https://doi.org/10.3390/solar2030020.
[67] R.T. Mouchou, et al., Numerical simulation and optimization of p-NiO/n-TiO2 solar cell system using SCAPS, Mater. Today Proc. 38 (2021) 835–841.
[68] M. Kumar Das, S. Panda, N. Mohapatra, Power conversion efficiency optimization of LaFeO3 Mott insulator based solar cell with metal oxide transport layers using SCAPS, Mater. Today Proc. (2022).

[69] S. Kamba, et al., Infrared and magnetic characterization of multiferroic $Bi_2FeCrO_6$ thin films over a broad temperature range, Phys. Rev. B 77 (10) (2008) 104111.
[70] Z. Yu, et al., Indium tin oxide as a semiconductor material in efficient p-type dye-sensitized solar cells, NPG Asia Mater. 8 (9) (2016) p. e305-e305.
[71] H. Zhong, et al., Investigation of the S-shaped current–voltage curve in high open-circuit voltage Ruddlesden–Popper perovskite solar cells, Front. Energy Res. 9 (2021).
[72] R. Saive, S-shaped current–voltage characteristics in solar cells: a review, IEEE J. Photovolt. 9 (6) (2019) 1477–1484.
[73] G. Wu, et al., Management of the crystallization in two-dimensional perovskite solar cells with enhanced efficiency within a wide temperature range and high stability, Nano Energy 58 (2019) 706–714.
[74] B. Qi, J. Wang, Fill factor in organic solar cells, Phys. Chem. Chem. Phys. 15 (23) (2013) 8972–8982.
[75] F. García-Sánchez, et al., Modelling solar cell S-shaped I-V characteristics with DC lumped-parameter equivalent circuits a review, Facta Univ. Ser. Electron. Energ. 30 (3) (2017) 327–350.
[76] A. Wagenpfahl, et al., S-shaped current-voltage characteristics of organic solar devices, Phys. Rev. B 82 (11) (2010) 115306.
[77] M.S. Bahrudin, . Jsc and Voc optimization of perovskite solar cell with interface defect layer using Taguchi method, in: Proceedings of the 2018 IEEE International Conference on Semiconductor Electronics (ICSE), 2018.
[78] K. Tan, et al., Controllable design of solid-state perovskite solar cells by SCAPS device simulation, Solid-State Electron. 126 (2016) 75–80.
[79] Y.-F. Gu, et al., Effect of carrier mobility on performance of perovskite solar cells*, Chin. Phys. B 28 (4) (2019) 048802.
[80] H. Lee, et al., Origin of open-circuit voltage reduction in high-mobility perovskite solar cells, Sol. Energy 236 (2022) 473–479.
[81] G. Wu, et al., Triphenylamine-based hole transporting materials with thiophene-derived bridges for perovskite solar cells, Synth. Met. 261 (2020) 116323.
[82] J. Park, et al., Unraveling doping capability of conjugated polymers for strategic manipulation of electric dipole layer toward efficient charge collection in perovskite solar cells, Adv. Funct. Mater. 30 (24) (2020) 2001560.
[83] S. Mabrouk, et al., Dithieno[3,2-b:2′,3′-d]pyrrole-based hole transport materials for perovskite solar cells with efficiencies over 18%, J. Mater. Chem. A 6 (17) (2018) 7950–7958.
[84] D.K. Jarwal, et al., Fabrication and TCAD validation of ambient air-processed ZnO NRs/CH3NH3PbI3/spiro-OMeTAD solar cells, Superlattices Microstruct. 143 (2020) 106540.
[85] Z. Wan, et al., A new strategy for constructing a dispiro-based dopant-free hole-transporting material: spatial configuration of spiro-bifluorene changes from a perpendicular to parallel arrangement, Chem. Sci. 12 (24) (2021) 8548–8555.
[86] M. Srivastava, et al., Highly efficient sandwich structured perovskite solar cell using PEDOT:PSS in room ambient conditions, Mater. Today Proc. 34 (2021) 675–678.
[87] J. Zhang, et al., Critical review of recent progress of flexible perovskite solar cells, Mater. Today 39 (2020) 66–88.